



**Accurate estimation of dynamical quantities for nonequilibrium nanoscale systems**Zhi Xu , Han Li, and Ming Ma <sup>\*</sup>*Department of Mechanical Engineering, State Key Laboratory of Tribology in Advanced Equipment (SKLT),  
Tsinghua University, Beijing 100084, China  
and Center for Nano and Micro Mechanics, Tsinghua University, Beijing 100084, China*

(Received 16 February 2022; accepted 9 December 2022; published 17 January 2023)

Fluctuations of dynamical quantities are fundamental and inevitable. For the booming research in nanotechnology, huge relative fluctuation comes with the reduction of system size, leading to large uncertainty for the estimates of dynamical quantities. Thus, increasing statistical efficiency, i.e., reducing the number of samples required to achieve a given accuracy, is of great significance for accurate estimation. Here we propose a theory as a fundamental solution for such problem by constructing auxiliary path for each real path. The states on auxiliary paths constitute canonical ensemble and share the same macroscopic properties (*NVT*) with the initial states of the real path. By implementing the theory in molecular dynamics simulations, we obtain a nanoscale Couette flow field with an accuracy of  $0.2 \mu\text{m/s}$  with relative standard error  $<0.1$ . The required number of samples is reduced by 12 orders compared to conventional method. The predicted thermolubric behavior of water sliding on a self-assembled surface is directly validated by experiment under the same velocity. This theory only assumes the system is initially in thermal equilibrium, then driven from that equilibrium by an external perturbation. It could serve as a general approach for extracting the accurate estimate of dynamical quantities from large fluctuations to provide insights on atomic level under experimental conditions, and benefit the studies on mass transport through (biological) nanochannels and fluid film lubrication of nanometer thickness.

DOI: [10.1103/PhysRevE.107.014124](https://doi.org/10.1103/PhysRevE.107.014124)**I. INTRODUCTION**

During the past decades, the scale of the systems people are interested in keeps on decreasing, from micro-, nano-, to angstrom, with typical applications like water desalination, nanopore sequencing, and heat dissipation of the chip [1–4]. This trend leads to the number of particles constituting the system,  $N$ , reducing significantly as it is proportional to the cubic of the scale. It also leads to large relative fluctuation (RF) of the dynamical quantities of the systems which is inverse proportional to the square root of  $N$  [5]. As a result, the standard error (SE) of the mean estimate for dynamical quantity  $A$  with multiple measurements ( $\bar{A}$ ) is large. In other words, the confidence intervals [ $\bar{A}-\text{SE}$ ,  $\bar{A}+\text{SE}$ ] from numerous samples that encompass the exact value of  $A$  with a probability of 68% are broad, leading to large uncertainties in the measurement. Thus, the intrinsic large RF brings difficulty to the estimate of the dynamical quantity for both experiments [6,7] and simulations [8–10] with nanoscale systems.

The conventional method uses the path-ensemble average to estimate the quantity at nonequilibrium. The accuracy of the estimate is limited by finite sampling. To increase the accuracy of the estimate, several strategies have been proposed. First, since SE is inverse proportional to the square root of the number of independent samples ( $n$ ), i.e.,  $\text{SE} \propto 1/\sqrt{n}$ , some methods increase  $n$  to get a good estimation, like using parallel replica dynamics with rare events [11], reducing the

cost of single sampling [12]. Second, some studies lead to a practical closed-form solution for the uncertainty of the estimation [13,14] and present new sampling algorithms to increase the statistical efficiency by one to three orders of magnitude. Third, as the statistical uncertainty of an estimator is usually quantified by its SE in the asymptotic limit, some studies find an optimal estimator [15,16] which reduces this asymptotic SE. These studies could increase the statistical efficiency by three orders.

With these methods, however, for nanoscale system with large RF, a large quantity of sampling is still required to provide enough data to get accurate estimate, e.g., with relative standard error (RSE)  $<0.1$  [9,17]. As for water, Fig. 1(a) shows the RF of the center-of-mass velocity ( $v_{\text{com}}$ ) varies with the number of particles  $N$  at room temperature ( $T = 298 \text{ K}$ ). For a steady water flow,  $\text{RF} = \sigma_{v_{\text{com}}}/v_{\text{com}}$ , where  $\sigma_{v_{\text{com}}} = \sqrt{1/\beta N m_{\text{water}}}$ ,  $\beta = 1/k_{\text{B}}T$ , and  $m_{\text{water}}$  is the mass of individual water molecule. Derivation of  $\sigma_{v_{\text{com}}}$  is given in Supplemental Material (SM), Sec. 1 [18]. With  $v_{\text{com}} = 10^{-4} \text{ m/s}$ , which is a typical value for experiments [17], it is clear that RF at nano- or angstrom scale is huge ( $>10^4$ ). For water flow at nanoscale (e.g.,  $N = 10000$ ), Fig. 1(b) illustrates with the first kind of method how many independent samples ( $n$ ) are required to detect certain values of  $v_{\text{com}}$  with a given RSE at  $T = 298 \text{ K}$ . Here,  $\text{RSE} = \sigma_{v_{\text{com}}}/\sqrt{nv_{\text{com}}}$  is used to measure the reliability of the estimate as the confidence interval is  $[1 - \text{RSE}, 1 + \text{RSE}]v_{\text{com}}$ , i.e., small RSE leading to accurate estimation. The number of samples needed to give an accurate estimate of  $v_{\text{com}} = 10^{-4} \text{ m/s}$  is five to seven orders larger than that in the existing research [9,35–39]. For

<sup>\*</sup>maming16@tsinghua.edu.cn

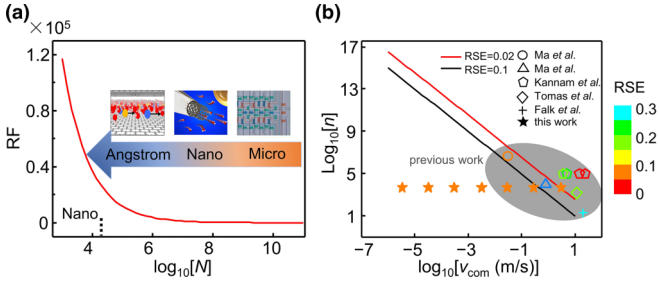


FIG. 1. Number of samples needed to estimate the flow rate of the nanoconfined water. (a) Relative fluctuation (RF) as a function of the number of particles  $N$  in the system. Arrow shows the recent experimental systems from micro- [40], nano- [41], to angstrom [42] scale, and the dashed line indicates the number of water molecules in a cube with a side length of 100 nm. (b) Number of independent samples  $n$  needed to estimate the velocity  $v_{\text{com}}$  with given relative standard error (RSE). Values of  $v_{\text{com}}$  for nanoconfined water in existing molecular simulations (0.03 to 24.3 m/s) and this work ( $3.36 \times 10^{-6}$  to 3 m/s) are plotted as different symbols.

the second and third kinds of methods as mentioned above, though they can increase the statistical efficiency up to three orders, the required number of samples would still be two to four orders larger than existing studies, far beyond the current ability of sampling. Therefore, for water at nanoscale, the existing methods to get accurate estimate of  $v_{\text{com}}$  comparable to experiments (e.g.,  $10^{-4}$  m/s) are inefficient and become even impractical.

In this paper, we propose a fundamentally different method to efficiently reduce the standard error of the estimate for dynamical quantities at nonequilibrium. Through generating an auxiliary path corresponding to each path in the phase space with a specific protocol, the path-ensemble average of the difference between the quantities in real path and auxiliary path is found to be a good estimate of the quantities. This method is thus called auxiliary-path method (APM). For achieving the same accuracy, the number of samples required for APM is much smaller than the conventional method.

## II. AUXILIARY-PATH METHOD

For a classical system composed of  $N$  particles, a dynamical quantity  $A$  depends upon time  $t$  via the time dependence of the coordinates  $\mathbf{r}_1(t), \dots, \mathbf{r}_N(t)$  and momenta  $\mathbf{p}_1(t), \dots, \mathbf{p}_N(t)$  of the particles, i.e.,  $A(t) = A[\mathbf{r}_1(t), \dots, \mathbf{r}_N(t), \mathbf{p}_1(t), \dots, \mathbf{p}_N(t)]$ . For each path, the phase-space point  $x_t \equiv [\mathbf{r}_1(t), \dots, \mathbf{r}_N(t), \mathbf{p}_1(t), \dots, \mathbf{p}_N(t)]$  is determined by integrating Newton's laws from the initial microstate ( $t = 0$ ) with the corresponding phase-space point  $x_0 \equiv [\mathbf{r}_1(0), \dots, \mathbf{r}_N(0), \mathbf{p}_1(0), \dots, \mathbf{p}_N(0)]$ , i.e., the dynamics of the system is deterministic. The exact value of  $A$  at time  $t$ ,  $\langle A \rangle_t$ , can be defined via path-ensemble average as  $\langle A \rangle_t = \int dx_0 F(x_0) A(t)$ , where  $F(x_0)$  is the distribution function of initial microstates in phase space [43]. In this paper, the path ensemble is constituted by the initial thermal equilibrium and the process by which the system is subsequently perturbed from that equilibrium as suggested by Crooks [44]. For system initially corresponding to canonical ensemble,  $F(x_0) = e^{-\beta H(x_0)} / \int dx_0 e^{-\beta H(x_0)}$ ,  $\beta = 1/k_B T$ , and  $H(x_0)$  is

the Hamiltonian of the initial microstate. For  $Q$  initial microstates correspond to a given sampling of the canonical phase-space distribution of a system; upon perturbation, they will generate  $Q$  nonequilibrium paths as time propagates. Thus, we have  $\langle A \rangle_t = \lim_{Q \rightarrow \infty} \frac{1}{Q} \sum_{i=1}^Q A_i(t)$  [45], where  $i$  indicates the  $i$ th path. While  $\langle A \rangle_t$  is the value people are interested in, practical sampling hardly fulfills ergodicity in the path ensemble. Therefore, the conventional method usually uses finite  $m$  paths in the path ensemble to estimate  $\langle A \rangle_t$  as  $\bar{A}_m(t) = \frac{1}{m} \sum_{i=1}^m A_i(t)$ , with  $\langle A \rangle_t = \lim_{m \rightarrow \infty} \bar{A}_m(t)$ . According to central limit theorem, the standard error of  $\bar{A}_m(t)$  can be estimated as  $\sigma_A / \sqrt{m}$ , where  $\sigma_A$  is the standard deviation of quantity  $A$ .

Now assuming that for the same system we have auxiliary path corresponding to each path in the nonequilibrium path ensemble, and the states  $x'_t \equiv [\mathbf{r}'_1(t), \dots, \mathbf{r}'_N(t), \mathbf{p}'_1(t), \dots, \mathbf{p}'_N(t)]$  on all auxiliary paths are required to constitute canonical ensemble at any time  $t$  when  $Q$  goes to infinity. Now we define a quantity  $B(t) = A(t) - A'(t)$ , here  $A'(t) = A(x'_t)$ . The path-ensemble average  $\langle B \rangle_t = \lim_{Q \rightarrow \infty} \frac{1}{Q} \sum_{i=1}^Q (A_i(t) - A'_i(t)) = \lim_{Q \rightarrow \infty} \frac{1}{Q} \sum_{i=1}^Q A_i(t) - \lim_{Q \rightarrow \infty} \frac{1}{Q} \sum_{i=1}^Q A'_i(t)$ . For the former,  $\lim_{Q \rightarrow \infty} \frac{1}{Q} \sum_{i=1}^Q A_i(t) = \langle A \rangle_t$ . For the latter, according to the assumption that the auxiliary states  $x'_t$  constitute canonical ensemble at any time  $t$ , we have  $\lim_{Q \rightarrow \infty} \frac{1}{Q} \sum_{i=1}^Q A'_i(t) = \langle A \rangle_{\text{EC}}$ , where  $\langle A \rangle_{\text{EC}}$  is the canonical ensemble average of  $A$ . Thus,  $\langle B \rangle_t = \langle A \rangle_t - \langle A \rangle_{\text{EC}}$ , i.e.,

$$\langle A \rangle_t = \langle B \rangle_t + \langle A \rangle_{\text{EC}}. \quad (1)$$

This is the proposed calculation method of  $\langle A \rangle_t$ , and it is the core of APM. Its efficiency over the conventional method which estimates  $\langle A \rangle_t$  as  $\bar{A}_m(t) = \frac{1}{m} \sum_{i=1}^m A_i(t)$  can be quantified via a dimensionless quantity  $\gamma$  as

$$SE_{\text{APM}} = \gamma SE_{\text{con}}, \quad (2)$$

where  $SE_{\text{APM}}$  and  $SE_{\text{con}}$  are the standard error of APM and the conventional method, respectively. To achieve the same SE, the APM reduces the required number of samples by  $1/\gamma^2$  times compared to the conventional method due to  $SE \propto 1/\sqrt{n}$ . In other words, the statistical efficiency of APM is increased by  $1/\gamma^2 - 1$  times compared to that of conventional method. On the basis that the auxiliary paths satisfy the requirements, according to Eq. (1),  $\langle A \rangle_t$  can be estimated by the sum of  $\bar{B}_m(t) = \frac{1}{m} \sum_{i=1}^m B_i(t)$  and a known constant  $\langle A \rangle_{\text{EC}}$ . Now  $SE_{\text{APM}} = \sigma_B / \sqrt{m}$ , where  $\sigma_B$  is the standard deviation of quantity  $B$  and  $SE_{\text{con}} = \sigma_A / \sqrt{m}$ ; thus,  $\gamma = \sigma_B / \sigma_A$ . The quantity  $\sigma_B$  can be estimated as  $\sqrt{p \sum_{i=1}^m (B_i(t) - \bar{B}_m(t))^2 / m}$  and  $\sigma_A$  can be estimated as  $\sqrt{\sum_{i=1}^m (A_i(t) - \bar{A}_m(t))^2 / m}$ , resulting in  $\gamma = \sqrt{\frac{\bar{B}_m^2(t) - (\bar{B}_m(t))^2}{\bar{A}_m^2(t) - (\bar{A}_m(t))^2}}$ , where  $\bar{B}_m^2(t) = \frac{1}{m} \sum_{i=1}^m B_i^2(t)$  and  $\bar{A}_m^2(t) = \frac{1}{m} \sum_{i=1}^m A_i^2(t)$ . For systems with large relative fluctuation,  $\bar{A}_m^2(t) \gg (\bar{A}_m(t))^2$ ; thus,  $\gamma \approx \sqrt{\frac{\bar{B}_m^2(t) - (\bar{B}_m(t))^2}{\bar{A}_m^2(t)}} < \sqrt{\bar{B}_m^2(t) / \bar{A}_m^2(t)}$ . When  $B^2(t)$  is much smaller than  $A^2(t)$ ,  $\gamma \ll 1$ , which means  $SE_{\text{APM}}$  is much smaller than  $SE_{\text{con}}$ . Thus, the auxiliary path method, i.e., using  $\bar{B}_m(t) + \langle A \rangle_{\text{EC}}$  to

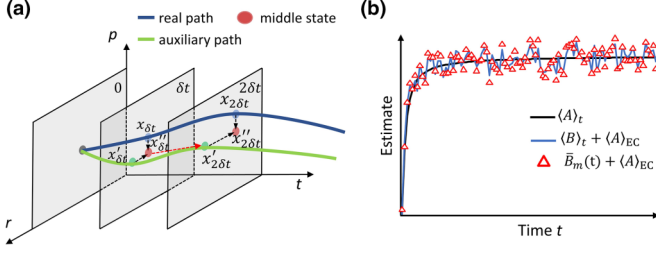


FIG. 2. Schematic of a specific protocol for APM. (a) The three axes are coordinate  $r$ , momentum  $p$ , and time  $t$ . The blue solid line stands for a real path in the nonequilibrium path ensemble with external perturbation and the green solid line is the corresponding auxiliary path. The black arrows reveal the origin of the middle states and the red arrow represents a relaxation with a duration of  $\delta t$ . (b) Schematic of the error analysis for the specific protocol. Two parts of error are introduced. One is the bias of  $\langle B \rangle_t + \langle A \rangle_{EC}$  (blue curve) from  $\langle A \rangle_t$  (black curve) caused by the finite  $\lambda$ . The other is the error caused by the estimation of  $\langle B \rangle_t + \langle A \rangle_{EC}$  with  $\bar{B}_m(t) + \langle A \rangle_{EC}$  (red triangles).

estimate  $\langle A \rangle_t$ , will be much more accurate than the conventional method, i.e., using  $\bar{A}_m(t)$  to estimate  $\langle A \rangle_t$ .

Generally speaking, the APM is done by designing auxiliary path corresponding to each real path in the nonequilibrium path ensemble. The requirements for the auxiliary paths are that the auxiliary states  $x'_t$  constitute canonical ensemble and share the same set of macroscopic properties, e.g., number and types of particles, volume, temperature, with the initial canonical ensemble at any time  $t$ . Based on both requirements, the closer the states on auxiliary path and real path are, the smaller  $\gamma$  is, and the more effective this method is.

### III. SPECIFIC PROTOCOL FOR APM

Next, we present a specific protocol to generate auxiliary path as shown in Fig. 2(a). Notice that the dynamics of the system remains unchanged; only the extra auxiliary paths are constructed to increase the accuracy of the estimate. We limit the studied systems as those which can preserve the canonical ensemble if having not been perturbed. At any given time  $t$ , there are three kinds of states, which are the real states  $x_t = [\mathbf{r}_1(t), \dots, \mathbf{r}_N(t), \mathbf{p}_1(t), \dots, \mathbf{p}_N(t)]$ , the states  $x'_t = [\mathbf{r}'_1(t), \dots, \mathbf{r}'_N(t), \mathbf{p}'_1(t), \dots, \mathbf{p}'_N(t)]$ , and the middle states  $x''_t$  which will be illustrated below. The basic steps of the protocol can be summarized as follows:

(1) At  $t = 0$ , the three types of states,  $x_t$ ,  $x'_t$ , and  $x''_t$ , are exactly the same and constitute canonical ensemble.

(2) Integrating the equations of motion forward in time under perturbation with a time step of  $\delta t$  to generate the real states  $x_{t+\delta t}$  from  $x_t$ .

(3) Integrating the equations of motion forward in time without perturbation to generate the states  $x''_{t+\delta t}$  from  $x''_t$ . Note that at  $t = 0$ ,  $x''_t$  and  $x_t$  are the same. At  $t > 0$ , nonequilibrium force for  $x''_t$  need be eliminated.

(4) The middle states  $x''_{t+\delta t}$  are obtained by combining the coordinate  $[\mathbf{r}_1(t + \delta t), \dots, \mathbf{r}_N(t + \delta t)]$  and the momentum

$[\mathbf{p}'_1(t + \delta t), \dots, \mathbf{p}'_N(t + \delta t)]$ , i.e.,  $[\mathbf{r}_1(t + \delta t), \dots, \mathbf{r}_N(t + \delta t), \mathbf{p}'_1(t + \delta t), \dots, \mathbf{p}'_N(t + \delta t)]$ .

(5) Update  $t$  to  $t + \delta t$  and repeat steps 2 to 4.

Then we will show that the states  $x'_t$  fulfill the requirement for auxiliary states approximately, i.e., they constitute canonical ensemble and share the same set of macroscopic properties with the initial canonical ensemble. Naturally at the beginning, both the states  $x'_0$  and  $x''_0$  constitute canonical ensembles as they are identical to  $x_0$ . For states  $x'_{\delta t}$ , as they are propagated from  $x'_0$  without any perturbation, they also constitute canonical ensemble, in other words, the probability of states  $x'_{\delta t}$ ,  $f(x'_{\delta t}) \propto e^{-\beta H(x'_{\delta t})}$ . Further, the essence of this protocol is a one-to-one correspondence between the real path and the auxiliary path; hence, each middle state  $x''_{\delta t}$  is determined by the auxiliary state  $x'_{\delta t}$  and its unique corresponding real state, which means  $f(x''_{\delta t}) = f(x'_{\delta t})$ . When the condition  $\lambda(\delta t) \rightarrow 0$  is met, where  $\lambda(\delta t) = \beta(\max_i \{\Delta H_i(\delta t)\} - \min_i \{\Delta H_i(\delta t)\})$ ,

$\Delta H_i(\delta t) = H_i(x'_{\delta t}) - H_i(x''_{\delta t})$ , we can derive that  $f(x''_{\delta t}) = \frac{e^{-\beta H(x''_{\delta t})}}{\sum_i e^{-\beta H(x''_{\delta t})}}$  (full derivation is given in SM, Sec. 2) [18]. It means

the states  $x''_{\delta t}$  satisfy canonical ensemble distribution function and thus constitute canonical ensemble. The auxiliary states  $x'_{\delta t}$  are obtained by a relaxation time of  $\delta t$  from the middle states  $x''_{\delta t}$ , and hence preserve the canonical ensemble. At this point, the construction implemented the auxiliary states from one moment ( $x'_{\delta t}$ ) to the next ( $x'_{2\delta t}$ ); as the construction goes on, we can get the auxiliary states  $x'_t$  at any time  $t$  when  $\lambda(t) \rightarrow 0$ .

With such protocol based on APM,  $\langle A \rangle_t$  can be estimated as  $\bar{B}_m(t) + \langle A \rangle_{EC}$ . As shown in Fig. 2(b), two parts of error are introduced. One is the bias of  $\langle B \rangle_t + \langle A \rangle_{EC}$  from  $\langle A \rangle_t$  caused by the finite  $\lambda$  which characterizes the approximation in the construction process of the auxiliary path. The other is the error caused by the estimation of  $\langle B \rangle_t + \langle A \rangle_{EC}$  with  $\bar{B}_m(t) + \langle A \rangle_{EC}$  due to the finite sampling. For the bias, when  $\lambda = 0$ , Eq. (1) shows  $\langle A \rangle_t = \langle B \rangle_t + \langle A \rangle_{EC}$ . However, the finite small  $\lambda$  will cause a bias of the auxiliary states away from the canonical ensemble. As a result, the upper limit of the bias is  $\sigma_A \sum_{j=1}^{C-1} \alpha^{C-j} \lambda(j\delta t)$ , where  $\alpha = e^{-\delta t/\tau}$ ,  $C$  is the number of time steps accumulated,  $t = C\delta t$ , and  $\tau$  is the relaxation time of the quantity  $A$  for a given system (full derivation is given in SM, Sec. 3) [18]. For the error caused by the estimation of  $\langle B \rangle_t + \langle A \rangle_{EC}$  with  $\bar{B}_m(t) + \langle A \rangle_{EC}$ , the confidence interval is  $[\bar{B}_m(t) + \langle A \rangle_{EC} - \frac{\sigma_B}{\sqrt{m}}, \bar{B}_m(t) + \langle A \rangle_{EC} + \frac{\sigma_B}{\sqrt{m}}]$ , where  $\frac{\sigma_B}{\sqrt{m}}$  is the standard error.

Therefore, for any instantaneous moment,  $\bar{B}_m(t) + \langle A \rangle_{EC}$  is a biased estimator of  $\langle A \rangle_t$  with the upper limit of the bias being  $\sigma_A \sum_{j=1}^{C-1} \alpha^{C-j} \lambda(j\delta t)$ . During the steady state where  $\langle A \rangle_t$  is a constant, however, the average of  $\bar{B}_m(t) + \langle A \rangle_{EC}$  calculated with  $C_s$  time steps  $\frac{1}{C_s} \sum_{C_s} \bar{B}_m(t) + \langle A \rangle_{EC}$  is an unbiased estimator due to the randomness of the bias between  $\langle B \rangle_t + \langle A \rangle_{EC}$  and  $\langle A \rangle_t$  (see details in SM, Sec. 3) [18]. According to central limit theorem, it has a standard error of  $\frac{1}{\sqrt{C_s}} (\frac{\sigma_B}{\sqrt{m}} + \sigma_A \sum_{j=1}^{C-1} \alpha^{C-j} \lambda(j\delta t))$ . With the same number of samples, the standard error for the conventional method of using  $\frac{1}{C_s} \sum_{C_s} \bar{A}_m(t)$  to estimate  $\langle A \rangle_t$  is  $SE_{con} =$

$\sigma_A/\sqrt{mC_s}$ . Therefore,  $\gamma = \sigma_B/\sigma_A + \sqrt{m} \sum_{j=1}^{C-1} \alpha^{C-j} \lambda(j\delta t)$ , and the times of increase in the statistical efficiency of this specific protocol for APM over conventional method can be estimated as  $\frac{1}{\gamma^2} - 1$ .

#### IV. TYPICAL APPLICATIONS

The auxiliary-path method brings us a powerful theoretical tool to obtain accurate estimate of dynamical quantities for nanoscale systems with intrinsically large relative fluctuations. This is particularly important for solid-liquid interface at nanoscale, as at room temperature the thermal fluctuation for liquid next to the solid surface is very large compared to the dynamical quantities people are interested in, e.g., flow rate. Among the many topics for solid-liquid interface, nanofluidics [46] and liquid superlubricity [47] have attracted great attention due to their great applications in energy and friction reduction. Therefore, we will take both cases as typical applications to demonstrate the ability of APM in increasing the statistical efficiency.

We first focused on a typical yet simple system where water is sheared by two parallel double-layer graphene sheets (homogeneous surfaces). Such a system [Fig. 3(a)] is a typical Couette flow, and it has profound significance in the field of nanofluidics. The length and width of the graphene layer are about 5 and 3 nm, respectively. The height of the channel is about 2.5 nm. The velocity of each water molecule is the dynamical quantity we are interested in. In the simulations, we use periodic boundary conditions in the  $x$ - and  $y$  directions parallel to the sheets and fixed boundary conditions in the  $z$  directions. The dimension of the simulation box in the  $z$  direction is 4 nm. A spring with stiffness of 2.7 N/m along the  $z$  direction was applied on each carbon atom in the top and bottom layers of graphene, connecting their present positions to their equilibrium positions. The water molecules were sheared by the graphene sheets moving at a constant velocity ( $V_{\text{wall}}$ ) in opposite directions along the  $x$  axis [Fig. 3(a)]. Electrostatic interaction between water molecules was modeled using the modified Wolf potential with damping parameter 0.2 [23]. With a long enough cutoff and small enough damping parameter, the energy and force calculated by the Wolf summation method approach those of the Ewald sum. A full description of the molecular dynamics (MD) simulation procedure is given in SM, Sec. 4 [18]. All the simulations were performed using LAMMPS [48] with a self-developed package incorporating the protocol for APM proposed above.

According to Eq. (1) for APM, the velocity field of water  $\langle \mathbf{v} \rangle_t = \lim_{Q \rightarrow \infty} \frac{1}{Q} \sum_{i=1}^Q (\mathbf{v}_i(t) - \mathbf{v}'_i(t)) + \langle \mathbf{v} \rangle_{\text{EC}}$ , where  $\mathbf{v}_i(t)$  is the velocity field of state  $x_t$  on the  $i$ th real path and  $\mathbf{v}'_i(t)$  is the velocity field of state  $x'_t$  on the corresponding auxiliary path. The equilibrium ensemble average of velocity field  $\langle \mathbf{v} \rangle_{\text{EC}} = 0$ . The perturbation to the water is the shear imposed by the moving graphene layers. With the same macroscopic properties, ten independent simulations were carried out at a given  $V_{\text{wall}}$ . During steady state, for each simulation, sampling over  $\mathbf{v}_i(t)$  and  $\mathbf{v}'_i(t)$  was conducted every 1 ps, lasting for 500 ps. These amount to a total number of samples of 5000 ( $m = 10$ ,  $C_s = 500$ ). Details of data analysis can be found in SM, Sec. 5 [18].

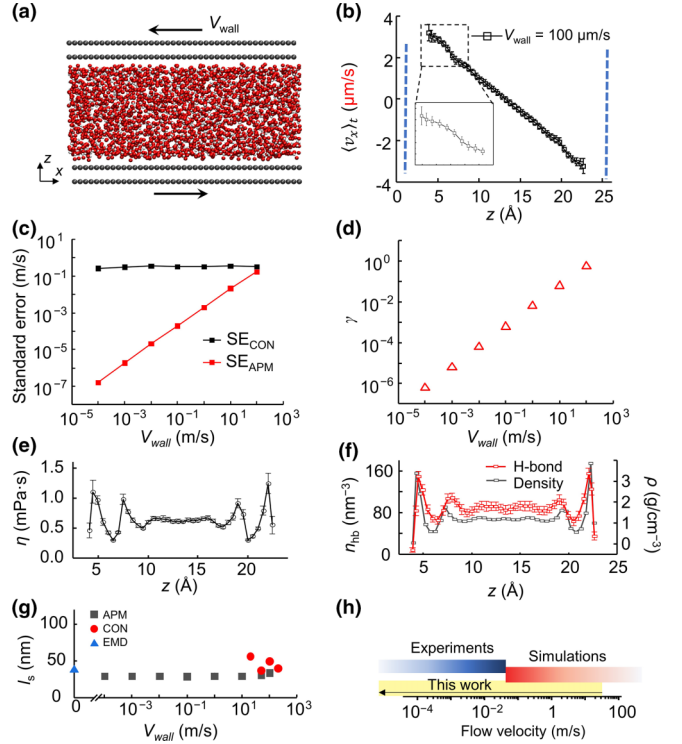


FIG. 3. Application of the specific protocol to nanoconfined water flow with homogeneous surfaces. (a) Side view of a typical studied system for water sheared by two double-layer graphene sheets. (b) Velocity profile of water flow obtained from APM with  $V_{\text{wall}} = 100 \mu\text{m/s}$ . Blue dotted lines are the average position of the innermost walls of graphene sheets. (c) Comparison between the standard error of velocity profiles obtained by the conventional method and APM with the same number of samples. (d) Ratio  $\gamma$  defined as  $\text{SE}_{\text{APM}}/\text{SE}_{\text{con}}$ . (e) Local viscosity  $\eta$  of water at different distance away from the innermost walls of graphene sheets. (f) Density of water  $\rho$  and the number density of hydrogen bond  $n_{\text{hb}}$  at different distance away from the innermost walls of graphene sheets. (g) Slip length ( $l_s$ ) vs  $V_{\text{wall}}$ . The  $x$  axis is composed of linear and logarithmic parts, separated by the break line. The only deviation is  $l_s$  based on the conventional method at  $V_{\text{wall}} = 20 \text{ m/s}$ , where the velocity profile is covered by the thermal noise. (h) Comparison of the flow velocity ranges studied in previous experiments ( $1 \times 10^{-6}$  to  $4 \times 10^{-2} \text{ m/s}$ ) [9], previous simulations ( $3 \times 10^{-2}$  to  $1000 \text{ m/s}$ ), [9,35–39], and the present work ( $3.36 \times 10^{-6}$  to  $3 \text{ m/s}$ ).

The profile along  $z$  of the flow velocity in the  $x$  direction ( $\langle v_x \rangle_t$ ) during steady state is shown in Fig. 3(b). It is worth noting that for  $V_{\text{wall}} = 100 \mu\text{m/s}$ , an accuracy of  $0.2 \mu\text{m/s}$  with  $\text{RSE} < 0.1$  was obtained for  $\langle v_x \rangle_t$ . This is a low velocity reported for water flow examined by MD, four orders smaller than existing studies ( $> 0.03 \text{ m/s}$ ) [9]. To understand why we could obtain such a low flow velocity with high accuracy, we calculated the corresponding  $\text{SE}_{\text{con}}$  and  $\text{SE}_{\text{APM}}$  as  $\sigma_{v_x}/\sqrt{mC_s}$  and  $\frac{1}{\sqrt{C_s}} \left( \frac{\sigma_{v_x - v'_x}}{\sqrt{m}} + \sigma_{v_x} \sum_{j=1}^{C-1} \alpha^{C-j} \lambda(j\delta t) \right)$ , respectively. The correspondence to Eq. (1),  $\langle A \rangle_t = \langle B \rangle_t + \langle A \rangle_{\text{EC}}$ , is  $v_x$  being  $A$  and  $v_x - v'_x$  being  $B$ . The values of  $\sigma_{v_x}$  and  $\sigma_{v_x - v'_x}$  were obtained from the simulations, with  $m = 10$ ,  $C_s = 500$ , and  $\alpha = e^{-t/\tau}$ , where  $t = 1 \text{ fs}$  and  $\tau = 0.1 \text{ ps}$  for the velocity

relaxation time of water molecule with simple point charge effective (SPC/E) force field [49]. From Fig. 3(c), it is evident that  $SE_{APM}$  is much smaller than  $SE_{con}$  for  $V_{wall} < 10$  m/s. For  $\gamma = SE_{APM}/SE_{con}$ , it reduces as  $V_{wall}$  decreases [Fig. 3(d)]. It is worth noting that with  $V_{wall} = 100 \mu\text{m/s}$ ,  $\gamma = 6.1 \times 10^{-7}$ . In other words, the APM reduces the required number of samples by  $2.2 \times 10^{12}$  ( $1/\gamma^2$ ) times compared to the conventional method, i.e., achieves a 12-order increase in statistical efficiency. It is worth noting that to obtain a velocity profile as shown in Fig. 3(b), the conventional method would take 74 billion yr with a CPU core running at 2.9 GHz, which is far beyond the present computing power (see SM, Sec. 8 for more details of the estimation) [18].

Such a high accuracy provides us an opportunity to examine the fine structure of the flow field at nanoscale. The linear profile [Fig. 3(b)], away from the boundary region (0.7 nm away from the graphene specifically [35,50]), is met with the classical prediction of planar Couette flow. However, we found a slight but clear oscillation of  $\langle v_x \rangle_t$  for water close to the surface [the inset of Fig. 3(b)] thanks to the high accuracy of APM. The oscillation of velocity at interface has been found in simulations of simple fluid with a large shear rate ( $10^{11} \text{ s}^{-1}$ ) [51,52]. For water, the shear rate studied here is  $4 \times 10^4 \text{ s}^{-1}$ , which is matched with the shear rate used in experiments ( $10^4$  to  $3 \times 10^5 \text{ s}^{-1}$ ) [53,54].

In Fig. 3(e), we plotted the local viscosity  $\eta(z) = \tau / \frac{d\langle v_x \rangle_t}{dz}$ , where  $\tau$  is the shear stress that holds constant in the stable flows. Previous studies [35,50] have found that the viscosity of water at the interface deviates from that of the bulk phase, but the detailed distribution remains unknown. The theory [51,55] for the viscosity distribution of confined Lennard-Jones fluid has been established using the local average density model [56]. Thanks to the accurate velocity profile from the APM [Fig. 3(b)], we achieved the quantitative calculation of viscosity distribution for nanoconfined water (see the calculation details in SM, Sec. 6) [18]. The oscillation of viscosity in the boundary region has a period of 0.25 nm, consistent with that of the density for water [Fig. 3(f)]. The viscosity of nanoconfined water has a 4 times variation, ranging from 0.30 to 1.25 mPa s. This is different from the results of applying local average density model with water [55]. Such difference shows that the local average density model may be not suitable for confined water of which the viscosity is not only affected by density but also by structure [e.g., the distribution of hydrogen bonds as shown in Fig. 3(f)] [57].

The accurate velocity profile [Fig. 3(b)] also enables us to calculate the slip length ( $l_s$ ), which is a typical quantity characterizing the flow profile and resistance at the liquid-solid interface [58]. The method in Ref. [59] for calculating  $l_s$  was used here,  $l_s = v_{slip}/\dot{\gamma}$ , where  $v_{slip}$  is the slip velocity and  $\dot{\gamma} = (d\langle v_x \rangle_t/dz)_{bulk}$  is the shear rate within the bulk region of the confined water. The slip velocity was obtained as the difference between  $V_{wall}$  and the linear extrapolated bulk velocity at the hydrodynamic wall position (HWP)  $V_{HWP}$ , i.e.,  $v_{slip} = V_{wall} - V_{HWP}$  (details about  $l_s$  calculation are given in SM, Sec. 7) [18]. During steady state, for  $V_{wall} = 50$  and  $100$  m/s, the estimated  $l_s$  using APM ( $30.8 \pm 0.7$  and  $34.1 \pm 1.0$  nm, respectively) is similar to that from the conventional method ( $37.3 \pm 8.7$  and  $50.0 \pm 13.2$  nm, respectively) as shown in

Fig. 3(g), confirming the validity of using APM in nanofluidics.

The dependence of  $l_s$  on  $v_{slip}$  is a key property in nanofluidics [60]. Based on transition-state theory,  $l_s$  is predicted to be a constant at water-carbon surface when  $v_{slip}$  is relatively low, e.g., less than 100 m/s [37]. Such a prediction has been verified by experiments and MD simulations separately. However, the flow-rate ranges investigated deviate, by large, 20 to 60  $\mu\text{m/s}$  in experiments [41] and 3 to 30 m/s in MD simulations [38]. With the system shown in Fig. 3(a), we calculated  $l_s$  with  $v_{slip}$  from  $9.6 \times 10^{-5}$  to 97 m/s using APM during steady state, of which the corresponding flow rate range covers that of nanoconfined fluid in the experiments [9] [Fig. 3(h)]. As shown in Fig. 3(g), within such a wide range,  $l_s$  remains a constant ( $30.5 \pm 1.5$  nm). We further compared these values to  $l_s$  with  $v_{slip} = 0$ . The latter can be estimated using the equilibrium molecular dynamics (EMD) method [33] as  $l_s = \eta_m/\lambda$ , where  $\lambda$  is friction coefficient and  $\eta_m$  is the viscosity of water at bulk region (0.7 nm away from the innermost graphene). This value can be regarded as the low-speed limit of  $l_s$ . With EMD, we obtained  $\lambda = (1.9 \pm 0.03) \times 10^4 \text{ kg m}^{-2} \text{ s}^{-1}$ , resulting in  $l_s = 33 \pm 1$  nm with  $\eta_m = (6.3 \pm 0.2) \times 10^{-4} \text{ kg m}^{-1} \text{ s}^{-1}$ . The agreement between  $l_s$  predicted by APM ( $30.5 \pm 1.5$  nm) and by EMD ( $33 \pm 1$  nm with  $v_{slip} = 0$ ) shows the validity of the APM in low-speed limit. The value of  $l_s$  ( $30.5 \pm 1.5$  nm) also lies in the range measured experimentally (16 nm for graphene nanochannels [61] and 60 nm for graphite nanochannels [62]). Together with the comparison to the conventional method, it is reasonable to conclude that the APM method works in a vast range of slip velocity for nanofluidics. As a result, for the dependence of  $l_s$  on  $v_{slip}$ , by bridging the gap spanning over four orders between experiments [41] and simulations [38], we found that  $l_s$  is velocity independent when  $v_{slip} < 97$  m/s, which validates the theoretical predictions [41].

Couette flow and Poiseuille flow are two basic flows in fluid mechanics. The APM proposed also applies for Poiseuille flow, which is also a common scenario for nanofluidics. We focused on the same system where water is confined by two parallel double-layer graphene sheets, as shown in Fig. 4(a). Poiseuille flow was generated by an external pressure gradient  $\Delta P$ . The interactions between molecules and the settings for MD simulation were the same with the simulation of Couette flow [Fig. 3(a)].

By using APM, Poiseuille flow field was obtained under a pressure gradient  $\Delta P$  of 0.2 Pa/nm. The pressure gradient used here was matched with the experiments [41,42,63] (0.4 to 250 Pa/nm). The profile along  $z$  of the flow velocity in the  $x$  direction  $\langle v_x \rangle_t$  during steady state was shown in Fig. 4(b). A slip length  $l_s$  of  $31.8 \pm 3.4$  nm was calculated from the velocity profile using the method as Ref. [64] suggested. The value of  $l_s$  is consistent with the results from Couette flow ( $30.5 \pm 1.5$  nm) and equilibrium MD ( $33 \pm 1$  nm) calculations estimated above.

Thermal noise is too large to obtain the velocity profile under experimental pressure gradient for the conventional method. For the direct comparison of APM and conventional method, we here increased  $\Delta P$  to  $2 \times 10^6$  Pa/nm. The evolution of center-of-mass velocity  $v_{com}$  for water flow versus time  $t$  was shown in Fig. 4(c). It is clear that the fluctuation

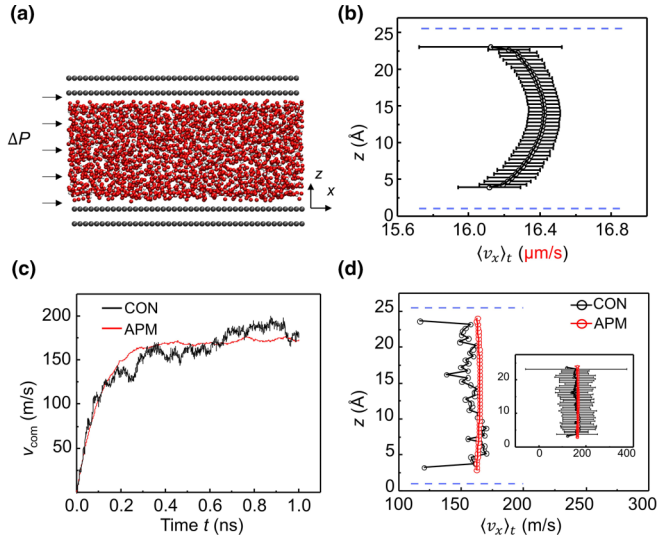


FIG. 4. Comparison of APM and conventional method for Poiseuille flow. (a) Side view of a typical studied system for water flow generated by a pressure drop  $\Delta P$ . (b) Velocity profile of water flow obtained from APM with  $\Delta P = 0.2$  Pa/nm. Blue dotted lines are the average position of the innermost walls of graphene sheets. (c) Center-of-mass velocity  $v_{\text{com}}$  vs time  $t$ . (d) Velocity profile of water flow obtained from APM with  $\Delta P = 2 \times 10^6$  Pa/nm. Blue dotted lines are the average position of the innermost walls of graphene sheets. Inset includes the standard error of velocity profile.

of  $v_{\text{com}}(t)$  calculated with APM is smaller than that calculated with conventional method. Besides, APM shows a more accurate velocity profile, as shown in Fig. 4(d). Through the direct comparison of velocity field calculated from APM and conventional method at a huge  $\Delta P$ , we show the effectiveness of APM on increasing statistical efficiency and the validity under huge external perturbation. At the experimental  $\Delta P$ , conventional method is struggling to obtain enough samples to reduce thermal fluctuation and APM shows unique ability on flow-field visualization.

Besides nanofluidics, the other typical example application of APM is liquid superlubricity. We studied the sliding of water on FDTS (Perfluorodecyltrichlorosilane,  $\text{C}_{10}\text{H}_4\text{C}_{13}\text{F}_{17}\text{Si}$ ) monolayer (heterogeneous surfaces). Such a system shows good superlubric properties among the many systems of liquid superlubricity [65]. However, the dependence of friction coefficient  $\lambda$  where  $\tau = \lambda v_{\text{slip}}$  on temperature remains unclear. Such dependence is important not only for the fundamental understanding of the physical mechanisms of slip at the interface, but also for applications like bearings and cooling of electronic devices.

Here, we constructed a MD simulation model considered water (a thickness of 3 nm) confined by FDTS monolayer and amorphous silica microsphere, as shown in Fig. 5(a). The silica surface, with a lateral size of  $4.5 \times 4.5 \text{ nm}^2$ , sheared the water molecules with a constant velocity  $U$ . The details of the simulation are presented in SM, Sec. 4 [18]. By using the APM, the velocity profiles of water flow were obtained with  $U$  from 30 to  $54 \mu\text{m/s}$  and temperature  $T$  from 298 to 348 K (see Fig. S4 in SM, Sec. 5) [18]. Then the local viscosity distribution was calculated using the same process

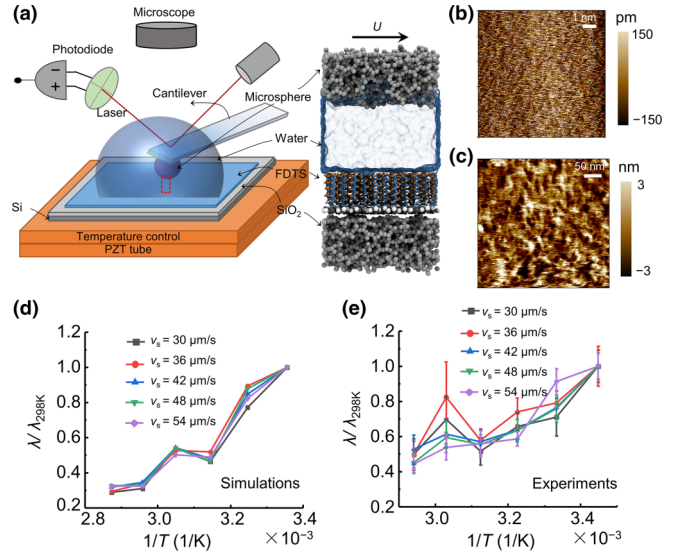


FIG. 5. Direct comparison between the temperature dependence of friction coefficient measured in experiments and predicted by APM. (a) Schematic of the setup to measure friction coefficient at water-FDTS interface in experiments (left) and MD simulations (right). Area highlighted by the dotted red rectangle is the system simulations considered. (b) Morphology characterization of the FDTS monolayer surface, with root-mean-square (rms) roughness of 0.08 nm for a  $10 \times 10 \text{ nm}^2$  area. (c) Morphology characterization of the microsphere surface, with rms roughness of 1.12 nm for a  $400 \times 400 \text{ nm}^2$  area. (d), (e) Temperature dependence of friction coefficient normalized by the value at 298 K for MD simulations (d) and experiments (e) under the same shearing velocity ( $v_s$ ) range, i.e., 30 to  $54 \mu\text{m/s}$ .

as that in Fig. 3(e) (see Fig. S9 in SM, Sec. 6) [18]. The friction coefficient at water-FDTS interface  $\lambda = \eta_m/l_s$  can be calculated with the obtained velocity profiles and viscosity distribution, and its temperature dependence is plotted in Fig. 5(d).

To validate the temperature dependence of friction coefficient predicted by MD simulations using APM, a well-designed experiment was performed as shown in Fig. 5(a). The self-assembled FDTS monolayer was physically vapor deposited onto a silica surface. A microsphere was fixed on the atomic force microscope cantilever. The morphology of the FDTS monolayer [Fig. 5(b)] and microsphere [Fig. 5(c)] indicated clean surfaces. During the measurement, the FDTS monolayer and the microsphere were immersed into degassed deionized water (18.2 M $\Omega$ , Hitech Sciencetool). The details of the measuring process are presented in SM, Sec. 9 [18]. During the measurement, the FDTS surface approached the microsphere with a constant normal velocity from 50 to  $90 \mu\text{m/s}$ , resulting in a tangential shearing velocity from 30 to  $54 \mu\text{m/s}$  at the water-FDTS interface (derivation was given in SM, Sec. 9) [18]. The temperature  $T$  from 290 to 340 K was used in experiment. The same velocity and temperature ranges used in experiments and APM guarantee a direct comparison between their results. The separation  $D$  and hydrodynamic resistance  $F_D$  between the microsphere and FDTS surface were recorded during the measurement (see Fig. S13 in SM, Sec. 9) [18]. The interfacial friction coefficient can be calculated from

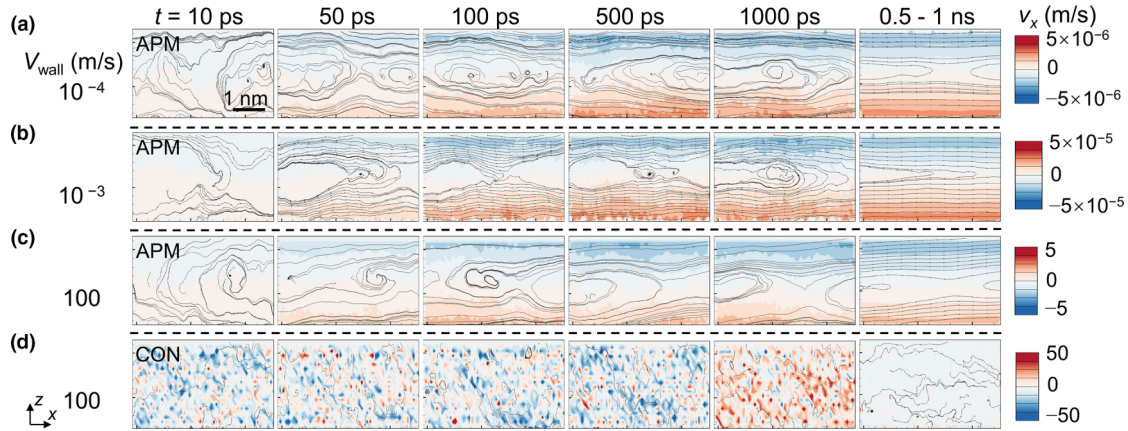


FIG. 6. Evolution of the flow field for water sheared by graphene. (a)–(c) Flow fields shown in the first three rows were obtained from the APM with  $V_{\text{wall}} = 10^{-4}$ ,  $10^{-3}$ , or 100 m/s. (d) Flow fields shown in the last row were obtained from the conventional method with  $V_{\text{wall}} = 100$  m/s. Streamlines which are a family of curves that are instantaneously tangent to the velocity vector of the flow were computed by the velocity field with a grid size of  $0.1 \text{ nm} \times 0.1 \text{ nm}$  (see SM, Sec. 5 for details) [18]. Movies S1–S4 corresponding to (a)–(d) are also provided as SM.

the  $F_D - D$  curves as suggested in Refs. [34,66,67] with results shown in Fig. 5(e).

Across the velocities studied, we observed clear thermolubric phenomena, i.e., the friction coefficient decreases with temperature [Figs. 5(d) and 5(e)]. With  $T$  increases from 298 to 348 K, by averaging  $\lambda$  over the cases for different velocities, the decrease in  $\lambda$  is found to be 67% in simulation and 55% by experiment, showing good agreement. This set of results based on a synergetic approach not only shows the thermolubric behavior for water on FDTS unambiguously, but also indicates rich information on atomic scale could be obtained to understand the mechanisms.

### V. DISCUSSION

One of the basic ideas of statistical mechanics is that we observe an average over all possibilities of dynamical quantity. This idea is corresponding to the notion of ensemble average in statistical physics, which was introduced by Gibbs in 1902 [68]. Path-ensemble average gives the value of nonequilibrium quantity by averaging states on the paths generated by applying external field on all states of the initial equilibrium ensemble. It is a natural corollary from ensemble average. The APM proposed is based on path-ensemble average, like many other theories in nonequilibrium statistical mechanics, such as Jarzynski nonequilibrium work relation [69], Onsager’s regression hypothesis [19], and path-ensemble theory [44].

With the APM, we show that one can extract an accurate estimate of the dynamical quantity from the huge relative fluctuations for system at nonequilibrium. For the conventional method, its standard error of the estimate is caused by two parts. One is the fluctuation of the initial equilibrium states. The other is the coupling between perturbation and equilibrium states. For APM, by using  $\langle \rangle_{\text{EC}}$ , the effect of the fluctuation of the initial equilibrium states on the estimate can be greatly suppressed. Meanwhile, the effect of the coupling between perturbation and equilibrium states on the estimate

remains unchanged. Benefit from this property, as shown below, the evolution of the dynamical quantities under external perturbation can be observed clearly.

In Figs. 6(a)–6(c), with APM we plot the evolution of the velocity fields for water sheared by the graphene sheets using the same model as shown in Fig. 3(a). Details of the flow-field calculation are given in SM, Sec. 5 [18]. The streamlines which are a family of curves that are instantaneously tangent to the velocity vector of the flow were computed by using the velocity fields. At any instantaneous moment, the fluctuation of the molecular velocity drives the flow field away from the typical estimation of Stokes flow, of which the streamlines should be parallel with the shearing wall strictly. The steady flow fields (the last column in Fig. 6) which were obtained by sampling the instantaneous flow field every 1 ps, then averaged over 500 ps during the steady state, however, show a good agreement with the prediction of Stokes flow. Compared with the flow field calculated by conventional method [Fig. 6(d)], it is evident that the APM can show the details of the flow field’s evolution at atomic scale, with flow velocity down to a few  $\mu\text{m/s}$ .

### VI. CONCLUSION

To conclude, we developed a theory which can give the accurate estimate of dynamical quantities for systems with huge fluctuations at nonequilibrium. This is done by the construction of auxiliary path for each real path in the phase space. The states on auxiliary paths constitute canonical ensemble and share the same macroscopic properties with the initial states of the real path. Taking nanofluidics as the first example, we demonstrated a 12-order of magnitude increase with APM in the statistical efficiency for the estimation of flow velocity. As a result, the proposed auxiliary-path method can obtain flow fields with a spatial precision of 0.1 nm and temporal resolution of 10 ps, for flow rate down to a few  $\mu\text{m/s}$ , which is within the reach of practical experiments [17,70]. Indeed, this is validated by the direct comparison between the friction

coefficients measured in experiment and estimated by APM where water is sliding on FDTS surface. Therefore, it is reasonable to expect a series of discoveries for nanofluidics and liquid lubrication with synergetic study by combining APM and experiments together.

On a broader scope, the APM theory only assumes that the system is initially in thermal equilibrium, then driven from that equilibrium by an external perturbation, and the dynamics of the system is deterministic. These two general assumptions pose little limitation on the applicable range of the theory. Therefore, the APM could serve as a general approach to provide insights on atomic level under experimental conditions. The specific protocol further assumes that if the system is unperturbed, then it preserves equilibrium ensemble. We

expect that with further developments in the construction of the auxiliary path, the gap between atomic simulations and experiments can be filled for fields like sliding between solid surfaces, the mass transport on nanoscale driven by chemical potential drop, and the multiphase flow under extreme confinements.

#### ACKNOWLEDGMENTS

M.M. acknowledges the support from the NSFC (Grants No. 11890673, No. 11772168, and No. 51961145304), National Supercomputer Center in Tianjin and Supercomputer Tansuo 100 of Tsinghua University, and the Shenzhen fundamental research key Project No. JCYJ20200109150608043.

- 
- [1] R. van Erp, R. Soleimanzadeh, L. Nela, G. Kampitsis, and E. Matioli, *Nature (London)* **585**, 211 (2020).
- [2] M. Jain *et al.*, *Nat. Biotechnol.* **36**, 338 (2018).
- [3] R. K. Joshi, P. Carbone, F. C. Wang, V. G. Kravets, Y. Su, I. V. Grigorieva, H. A. Wu, A. K. Geim, and R. R. Nair, *Science* **343**, 752 (2014).
- [4] A. Vanossi, N. Manini, M. Urbakh, S. Zapperi, and E. Tosatti, *Rev. Mod. Phys.* **85**, 529 (2013).
- [5] L. D. Landau and E. M. Lifshitz, in *Statistical Physics*, 3rd ed. (Butterworth-Heinemann, Oxford, 1980), p. 6.
- [6] D. Collin, F. Ritort, C. Jarzynski, S. B. Smith, I. Tinoco, and C. Bustamante, *Nature (London)* **437**, 231 (2005).
- [7] P. Maragakis, F. Ritort, C. Bustamante, M. Karplus, and G. E. Crooks, *J. Chem. Phys.* **129**, 024102 (2008).
- [8] S. K. Kannam, P. J. Davis, and B. D. Todd, *MRS Bull.* **42**, 283 (2017).
- [9] M. Ma, F. Grey, L. M. Shen, M. Urbakh, S. Wu, J. Z. Liu, Y. L. Liu, and Q. S. Zheng, *Nat. Nanotechnol.* **10**, 692 (2015).
- [10] M. Ma, G. Tocci, A. Michaelides, and G. Aeppli, *Nat. Mater.* **15**, 66 (2016).
- [11] A. F. Voter, *Phys. Rev. B* **57**, R13985 (1998).
- [12] P. Nicolini, D. Frezzato, and R. Chelli, *J. Chem. Theory Comput.* **7**, 582 (2011).
- [13] N. Singhal and V. S. Pande, *J. Chem. Phys.* **123**, 204909 (2005).
- [14] N. S. Hinrichs and V. S. Pande, *J. Chem. Phys.* **126**, 244101 (2007).
- [15] M. R. Shirts and J. D. Chodera, *J. Chem. Phys.* **129**, 124105 (2008).
- [16] D. D. L. Minh and J. D. Chodera, *J. Chem. Phys.* **131**, 134110 (2009).
- [17] X. C. Qin, Q. Z. Yuan, Y. P. Zhao, S. B. Xie, and Z. F. Liu, *Nano Lett.* **11**, 2173 (2011).
- [18] See Supplemental Material at <http://link.aps.org/supplemental/10.1103/PhysRevE.107.014124> for the formula derivations and the settings of simulations and experiments, which includes Refs. [19–34].
- [19] L. Onsager, *Phys. Rev.* **37**, 405 (1931).
- [20] Y. J. Wu, H. L. Tepper, and G. A. Voth, *J. Chem. Phys.* **124**, 024503 (2006).
- [21] D. W. Brenner, O. A. Shenderova, J. A. Harrison, S. J. Stuart, B. Ni, and S. B. Sinnott, *J. Phys.: Condens. Matter* **14**, 783 (2002).
- [22] T. Werder, J. H. Walther, R. L. Jaffe, T. Halicioglu, and P. Koumoutsakos, *J. Phys. Chem. B* **107**, 1345 (2003).
- [23] C. J. Fennell and J. D. Gezelter, *J. Chem. Phys.* **124**, 234104 (2006).
- [24] W. G. Ouyang, D. Mandelli, M. Urbakh, and O. Hod, *Nano Lett.* **18**, 6009 (2018).
- [25] S. Toxvaerd and J. C. Dyre, *J. Chem. Phys.* **134**, 081102 (2011).
- [26] H. Yoshida, V. Kaiser, B. Rotenberg, and L. Bocquet, *Nat. Commun.* **9**, 1496 (2018).
- [27] S. Bernardi, B. D. Todd, and D. J. Searles, *J. Chem. Phys.* **132**, 244706 (2010).
- [28] O. M. Roscioni, L. Muccioli, A. Mityashin, J. Cornil, and C. Zannoni, *J. Phys. Chem. C* **120**, 14652 (2016).
- [29] R. G. Dellavalle and H. C. Andersen, *J. Chem. Phys.* **97**, 2682 (1992).
- [30] H. J. C. Berendsen, J. R. Grigera, and T. P. Straatsma, *J. Phys. Chem.* **91**, 6269 (1987).
- [31] T. A. Ho, D. Argyris, D. V. Papavassiliou, A. Striolo, L. L. Lee, and D. R. Cole, *Mol. Simul.* **37**, 172 (2011).
- [32] Y. B. Xie, L. Fu, T. Niehaus, and L. Joly, *Phys. Rev. Lett.* **125**, 014501 (2020).
- [33] K. Huang and I. Szlufarska, *Phys. Rev. E* **89**, 032119 (2014).
- [34] O. I. Vinogradova, *Langmuir* **11**, 2213 (1995).
- [35] J. A. Thomas and A. J. H. McGaughey, *Nano Lett.* **8**, 2788 (2008).
- [36] K. Falk, F. Sedlmeier, L. Joly, R. R. Netz, and L. Bocquet, *Nano Lett.* **10**, 4067 (2010).
- [37] M. D. Ma, L. M. Shen, J. Sheridan, J. Z. Liu, C. O. Chen, and Q. S. Zheng, *Phys. Rev. E* **83**, 036316 (2011).
- [38] S. K. Kannam, B. D. Todd, J. S. Hansen, and P. J. Davis, *J. Chem. Phys.* **136**, 024705 (2012).
- [39] W. Xiong, J. Z. Liu, M. Ma, Z. P. Xu, J. Sheridan, and Q. S. Zheng, *Phys. Rev. E* **84**, 056329 (2011).
- [40] T. M. Squires and S. R. Quake, *Rev. Mod. Phys.* **77**, 977 (2005).
- [41] E. Secchi, S. Marbach, A. Nigues, D. Stein, A. Siria, and L. Bocquet, *Nature (London)* **537**, 210 (2016).
- [42] T. Mouterde, A. Keerthi, A. R. Poggioli, S. A. Dar, A. Siria, A. K. Geim, L. Bocquet, and B. Radha, *Nature (London)* **567**, 87 (2019).
- [43] D. Chandler, *Introduction to Modern Statistical Mechanics* (Oxford University Press, Oxford, 1987), Chap. 8.
- [44] G. E. Crooks, *Phys. Rev. E* **61**, 2361 (2000).



- [45] M. E. Tuckerman, *Statistical Mechanics: Theory and Molecular Simulation* (Oxford University Press, Oxford, 2010), Chap. 7.2.
- [46] L. Bocquet, *Nat. Mater.* **19**, 254 (2020).
- [47] T. Han, S. Zhang, and C. Zhang, *Friction* **10**, 1137 (2022).
- [48] S. Plimpton, *J. Comput. Phys.* **117**, 1 (1995).
- [49] M. Khademi and M. Sahimi, *J. Chem. Phys.* **135**, 204509 7,(2011).
- [50] K. L. Wu, Z. X. Chen, J. Li, X. F. Li, J. Z. Xu, and X. H. Dong, *Proc. Natl. Acad. Sci. USA* **114**, 3358 (2017).
- [51] H. Hoang and G. Galliero, *Phys. Rev. E* **86**, 021202 (2012).
- [52] Y. Y. Wang, J. B. Xu, S. Wang, and C. Yang, *Nanoscale* **9**, 6777 (2017).
- [53] L. Li, J. W. Mo, and Z. G. Li, *Phys. Rev. E* **90**, 033003 (2014).
- [54] X. Yu, Y. G. Meng, Y. Tian, J. Zhang, and W. B. Liang, *Tribol. Int.* **94**, 20 (2016).
- [55] R. Bhadauria, T. Sanghi, and N. R. Aluru, *J. Chem. Phys.* **143**, 174702 (2015).
- [56] I. Bitsanis, J. J. Magda, M. Tirrell, and H. T. Davis, *J. Chem. Phys.* **87**, 1733 (1987).
- [57] M. Neek-Amal, F. M. Peeters, I. V. Grigorieva, and A. K. Geim, *ACS Nano* **10**, 3685 (2016).
- [58] C. L. Navier, *Mémoires de l'Académie Royale des Sciences de l'Institut de France* **6**, 389 (1823).
- [59] C. Herrero, T. Omori, Y. Yamaguchi, and L. Joly, *J. Chem. Phys.* **151**, 041103 (2019).
- [60] L. Bocquet and E. Charlaix, *Chem. Soc. Rev.* **39**, 1073 (2010).
- [61] Q. Xie, M. A. Alibakhshi, S. P. Jiao, Z. P. Xu, M. Hempel, J. Kong, H. G. Park, and C. H. Duan, *Nat. Nanotechnol.* **13**, 238 (2018).
- [62] A. Keerthi, S. Goutham, Y. You, P. Iamprasertkun, R. A. W. Dryfe, A. K. Geim, and B. Radha, *Nat. Commun.* **12**, 3092 (2021).
- [63] A. Siria, P. Poncharal, A. L. Biance, R. Fulcrand, X. Blase, S. T. Purcell, and L. Bocquet, *Nature (London)* **494**, 455 (2013).
- [64] S. K. Kannam, B. D. Todd, J. S. Hansen, and P. J. Davis, *J. Chem. Phys.* **135**, 144701 (2011).
- [65] J. J. Li, W. Cao, J. F. Li, M. Ma, and J. B. Luo, *J. Phys. Chem. Lett.* **10**, 2978 (2019).
- [66] C. D. F. Honig and W. A. Ducker, *J. Phys. Chem. C* **111**, 16300 (2007).
- [67] C. Cottin-Bizonne, A. Steinberger, B. Cross, O. Raccurt, and E. Charlaix, *Langmuir* **24**, 1165 (2008).
- [68] J. W. Gibbs, *Elementary Principles in Statistical Mechanics* (Charles Scribner's Sons, New York, 1902).
- [69] C. Jarzynski, *Phys. Rev. Lett.* **78**, 2690 (1997).
- [70] M. Majumder, N. Chopra, and B. J. Hinds, *ACS Nano* **5**, 3867 (2011).